A new topological insulator built from quasi one-dimensional atomic ribbons

Piet Schönherr[1], Shilei Zhang[1], Yuanqian Liu[1, 2], Patryk Kusch[3], Stephanie Reich[3], Terence Giles[4], Dominik Daisenberger[4], Dharmalingam Prabhakaran[1], Yulin Chen[1], and Thorsten Hesjedal[*, 1]

[1] Department of Physics, Clarendon Laboratory, University of Oxford, Oxford OX1 3PU, United Kingdom
[2] University of Science and Technology of China, Hefei 230026, P.R. China
[3] Freie Universität Berlin, Fachbereich Physik, Arnimallee 14, 14195 Berlin, Germany
[4] Diamond Light Source, Chilton, Didcot, Oxfordshire, OX11 0DE, United Kingdom

[*] Corresponding author: e-mail t.hesjedal1@physics.ox.ac.uk

A novel topological insulator with orthorhombic crystal structure is demonstrated. It is characterized by quasi one-dimensional, conducting atomic chains instead of the layered, two-dimensional sheets known from the established $Bi_2(Se,Te)_3$ system. The Sb-doped Bi_2Se_3 nanowires are grown in a TiO_2-catalyzed process by chemical vapor deposition. The binary Bi_2Se_3 is transformed from rhombohedral to ortho-rhombic by substituting Sb on ~38% of the Bi sites. Pure Sb_2Se_3 is a topologically trivial band insulator with an orthorhombic crystal structure at ambient conditions, and it is known to transform into a topological insulator at high pressure. Angle-resolved photoemission spectroscopy shows a topological surface state, while Sb doping also tunes the Fermi level to reside in the bandgap.

1 Introduction Topological insulators (TIs) are fascinating quantum materials which are characterized by an insulating bulk and a conducting surface state [1–3]. The topological surface state (TSS) is protected by time-reversal symmetry and it is robust against scattering from non-magnetic impurities [4]. A bandstructure with an odd number of Dirac cones residing in the bulk bandgap is the signature of TIs [5]. Their characteristic that the charge carriers of opposite spin have opposite linear momentum makes TIs ideal systems for a range of possible spin-based and low-power electronic applications. Nanowires in general have a high surface-to-volume ratio, enhancing the relative contribution of the TSS to the overall electric transport in TI nanostructures [6–9]. The synthesis of one-dimensional structures most commonly relies on an Au-catalyzed vapor–liquid–solid (VLS) growth process [10–13], in which the catalyst forms a liquid alloy with the vapor, and the crystal growth occurs at the liquid–solid interface. Unfortunately, the migration of the Au catalyst and the subsequent deterioration of the electronic properties of the nanostructures are fundamental limitations for device applications [14]. However, TI nanostructures can also be grown in a catalyst-free process with low yield [15], or by

using TiO_2 catalysts which do not incorporate into the nanostructures, yet yield high uniformity and density [16].

Since the first experimental demonstration of a two-dimensional TI in the form of HgTe/(Hg,Cd)Te quantum wells [17], and the three-dimensional TIs Bi_xSb_{1-x} [18], Bi_2Se_3 [19, 20], and Bi_2Te_3 [20, 21], only a few more TIs were experimentally confirmed. In general, the search for novel TIs utilizes strain as a means to stabilize metastable phases as in case of Ag_2Te [22], or to open a bandgap in semimetals like α-Sn [23], and HgTe [24].

Bi_2Se_3 is in the focus of much experimental work owing to its large bulk bandgap and relatively simple single Dirac cone surface bandstructure. However, the bismuth sesquichalcogenides such as Bi_2Se_3 are plagued by chalcogen vacancies leading to intrinsic n-type doping, and thus to an increase of the Fermi level above the Dirac point. Sb doping was reported to suppress Se vacancies by substitution of Bi atoms in bulk samples [25], and MBE grown thin films [26]. Similar improvements are possible in nanowires grown using the VLS method [27]. In nanosheets, an Sb_2Se_3 guest lattice is formed at a doping level of 10% Sb and no further substitution on Bi sites is possible [28].

Phys. Status Solidi RRL **9**, No. 2 (2015)

131

Bi$_2$Se$_3$ which has been grown at ambient conditions usually has a rhombohedral crystal structure (space group R$\bar{3}$m) and at high pressure an orthorhombic crystal structure (space group Pnma) [29]. However, when quenching it from high-pressure growth conditions it remains metastable. The orthorhombic form of Bi$_2$Se$_3$ occurs naturally as well and is known as Guanajuatite [30]. Further, it has been reported that the orthorhombic phase can be induced by S and Sb doping [31, 32]. This is interesting in terms of TIs because of the reduced conductivity compared to the rhombohedral phase [33].

In contrast to the layered compounds of the Bi$_2$(Se,S,Te)$_3$ solid solution series, orthorhombic Bi$_2$Se$_3$ is characterized by a one-dimensional nanoribbon structure. The polymer-like [Bi$_4$Se$_6$]$_n$ chain is linked to four neighbors per unit via weak Bi–Se and Se–Se bonds [34]. Density functional theory simulations have shown an electronic quasi one-dimensional behavior as van Hove singularities are found in the density of states [35]. For orthorhombic Sb$_2$Se$_3$ it is reported that the surface of the (internal) nanoribbons, which are 0.2 nm thick and 1 nm wide, is virtually perfect due to the absence of dangling bonds [36].

Here, we present experimental evidence that orthorhombic (Bi$_{0.62}$Sb$_{0.38}$)$_2$Se$_3$ with its strong structural and electronic one-dimensional character is a topological insulator. Chemical vapor deposition (CVD) is used to grow high-density (Bi,Sb)$_2$Se$_3$ nanowires in a TiO$_2$ nanoparticle catalyzed process. We use X-ray diffraction (XRD) and transmission electron microscopy (TEM) to unambiguously identify the crystal structure and angle-resolved photoemission spectroscopy (ARPES) to confirm the existence of a TSS in this material.

2 Experimental

2.1 Synthesis Samples were grown in a horizontal, 60 cm long tube furnace (Nabertherm B180) equipped with a sealed, 22 mm inner diameter quartz tube. Substrates and precursor material were placed in quartz boats inside the tube. The precursor was prepared by grinding Sb-doped Bi$_2$Se$_3$ single crystals into a fine powder. Cleaned Si substrates were functionalized using the binding agent poly-l-lysine and a custom-made P-25 TiO$_2$ catalyst solution was applied [16]. Before loading the substrates the system was purged by repeated cycles of low vacuum pumping and dry N$_2$ flushing. Substrates were loaded under N$_2$ flow. N$_2$ was also used as the carrier gas and the flow rate was 150 sccm (standard cubic centimeters per minute). The furnace temperature in the center was ramped up to 585 °C for 60 min and held constant for 60 min. The substrates were placed approximately 25 cm away from the center in the upstream direction at gradually cooler spots. After the growth the furnace was switched off and allowed to cool down while keeping N$_2$ flowing.

2.2 X-ray characterization Nanowires were carefully scraped from the substrate and placed onto the culet of a single crystal diamond for X-ray powder diffraction

measurements on beamline I15 at Diamond Light Source. A pre-focused monochromatic beam (E = 37.06 keV) was collimated with a 30 μm pinhole. Powder diffraction patterns were recorded by a Perkin Elmer detector, integrated using Fit-2D [37], and analyzed using TOPAS [38].

2.3 Raman A Horiba T64000 Raman spectrometer system in combination with a HeNe laser (λ = 633 nm) was used for lower wavenumbers and a titanium–sapphire laser (λ = 800 nm) for higher wavenumbers. The backscattered light was collected through a 100× objective lens and dispersed by a triple grating spectrometer with a spectral resolution of 1 cm^{-1}. In this configuration we were able to study individual nanowires. The polarization of the light was parallel to the nanowire axis to maximize the intensity. All measurements were carried out at room temperature. The spectrometer was calibrated using a Ne standard.

2.4 ARPES Micro-ARPES measurements were conducted at the spectromicroscopy beamline at Elettra Synchrotron Radiation Laboratory in Italy on a single nanowire, with energy resolution at 70 meV and angle resolution 0.5°. The surface of the sample was cleaned by several cycles of Ar-sputtering.

3 Results

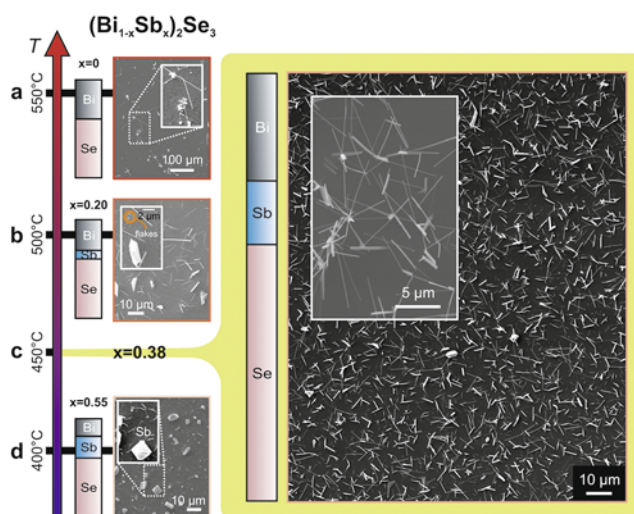Figure 1 shows scanning electron microscopy (SEM) images of the growth results as a function

Figure 1 Temperature-dependence of the (Bi$_{1-x}$Sb$_x$)$_2$Se$_3$ nanowire growth: (a) at 550 °C, thick Sb-free Bi$_2$Se$_3$ wires with diameters in the range of micrometers are grown alongside other Bi$_2$Se$_3$ structures; (b) at 500 °C the density of the wires is higher and the Sb is incorporated. The diameter of the (Bi$_{0.80}$Sb$_{0.20}$)$_2$Se$_3$ structures is on the order of hundreds of nm and the lengths around several μm. However, the structures are still a mixture of wires and plates. The flakes in the inset are an example of agglomerated catalyst material; (c) at 450 °C, (Bi$_{0.62}$Sb$_{0.38}$)$_2$Se$_3$ ribbons are found with a high density. Their diameter is 50–100 nm and their length a few μm; (d) at 400 °C Sb dominates over Bi and the stoichiometry of the nanowires is (Bi$_{0.45}$Sb$_{0.55}$)$_2$Se$_3$. Also, elemental Sb begins to crystallize out.

● Bi ● Se

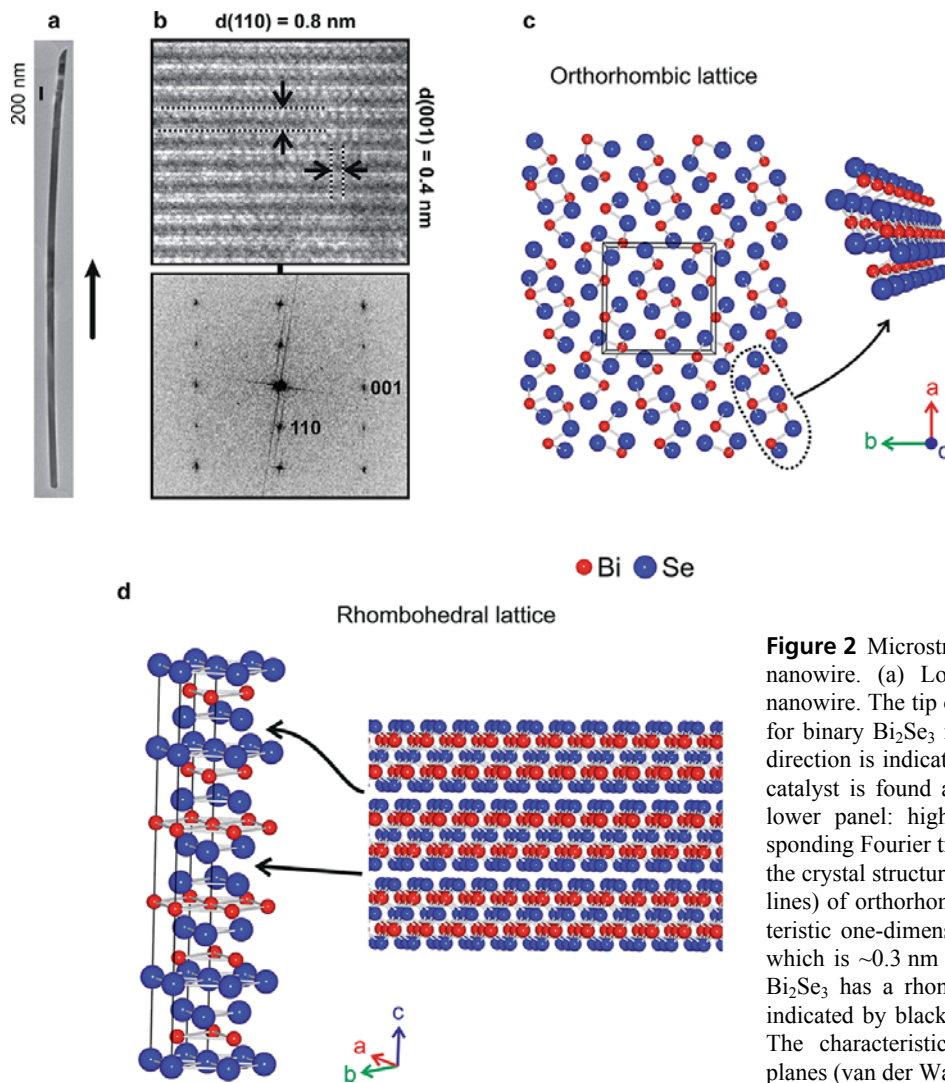**Figure 2** Microstructural analysis of a $(Bi_{0.62}Sb_{0.38})_2Se_3$ nanowire. (a) Low-magnification TEM image of a nanowire. The tip of the wire is slanted, which is typical for binary Bi_2Se_3 nanowires as well. The [001] growth direction is indicated by an arrow. No trace of the TiO_2 catalyst is found anywhere along the wire. (b) Upper/lower panel: high-resolution TEM image and corresponding Fourier transformation, respectively, show that the crystal structure is orthorhombic. (c) Unit cell (black lines) of orthorhombic Bi_2Se_3. On the right, the characteristic one-dimensional nanoribbon structure is shown which is ~0.3 nm thick and 1.1 nm wide. (d) Undoped Bi_2Se_3 has a rhombohedral crystal structure (unit cell indicated by black lines) and is shown for comparison. The characteristic two-dimensional, weakly bonding planes (van der Waals gap) are indicated by arrows.

of substrate temperature. High purity and density $(Bi_{0.62}Sb_{0.38})_2Se_3$ nanowires, which are the main focus of this investigation, grow at a substrate temperature of 450 °C. The furnace temperature was 600 °C for all growth experiments. Above a substrate temperature of 450 °C, sparsely distributed larger wires with a lower Sb concentration are found. For lower temperatures, less Bi is incorporated leading to the growth of Sb_2Se_3 nanowires and the appearance of Sb crystals. The Sb concentration is measured by SEM energy-dispersive X-ray spectroscopy (EDS) with an error of ~10 at%. A typical EDS spectrum is shown in the Supporting Information, Fig. S1. The nanowire growth depends on the catalyst particle size as can be seen in Fig. 1b, where large TiO_2 flakes have not catalyzed any material deposition. Below we present the study of the nanowires grown at 450 °C to determine the crystal structure and the electronic properties.

Pure Bi_2Se_3 has a rhombohedral lattice structure with space group $R\bar{3}m$ at ambient conditions. In high pressure experiments a metastable orthorhombic phase was ob-

served [39], which has the same crystal structure as Sb_2Se_3 (orthorhombic space group Pnma). Lattice-resolved TEM images (Fig. 2a) show that an orthorhombic phase forms upon Sb incorporation in Bi_2Se_3 nanowires. The interplanar spacings for $(Bi_{0.62}Sb_{0.38})_2Se_3$ are $d_{110} = 0.8$ nm and $d_{001} = 0.4$ nm and compare to 0.828 nm and 0.398 nm, respectively, for pure Sb_2Se_3 nanowires [40].

An ensemble of nanowires was investigated by X-ray powder diffraction at beamline I15 at Diamond Light Source (Didcot, Oxfordshire, England). The reader is reffered to the Supporting Information for details on the crystal structure analysis.). The dominating phase for $(Bi_{0.62}Sb_{0.38})_2Se_3$ is the orthorhombic phase which was identified in the diffraction pattern using the Rietveld method. Small amounts of the rhombohedral phase and Si are also present in the ensemble since the nanowires were obtained by scratching from a Si substrate. The fit to the data is presented in Fig. 3. Since the Sb concentration is not high enough to form pure Sb_2Se_3 structures to such a high percentage, we conclude that $(Bi_{0.62}Sb_{0.38})_2Se_3$ forms

Phys. Status Solidi RRL **9**, No. 2 (2015)

133

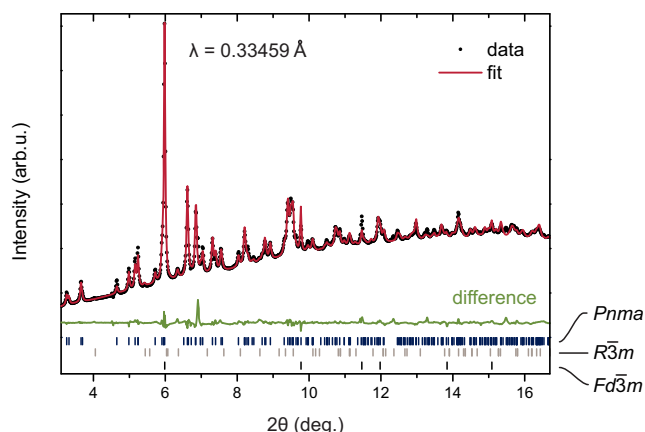**Figure 3** X-ray diffraction pattern of an ensemble of $(Bi_{0.62}Sb_{0.38})_2Se_3$ nanowires. The X-ray diffraction data (black dots) is the integrated X-ray intensity of the powder diffraction pattern. It is fitted by the dotted line using the Rietveld method with the software package TOPAS. The best fit (red line) is obtained for the orthorhombic phase and a small amount of rhombohedral material and Si (from the substrate). The green line shows the difference between the data and the fit. Expected peaks for the space group of the orthorhombic unit cell (Pnma, blue) and the rhombohedral unit cell ($R\bar{3}m$, grey) for Bi_2Se_3 are indicated at the bottom. Peaks for Si ($Fd\bar{3}m$, black) are also indicated.

an orthorhombic lattice. Bi atoms occupy Sb sites in the orthorhombic Sb_2Se_3-type lattice as we will see in the Raman spectrum.

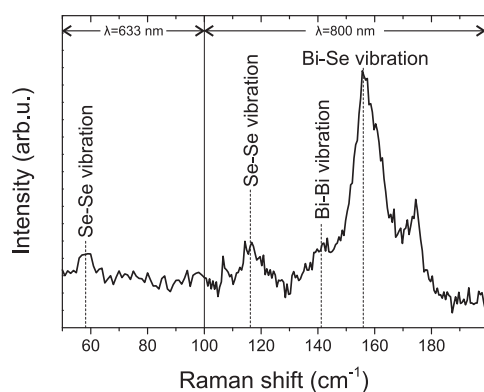The Raman spectrum of a single $(Bi_{0.62}Sb_{0.38})_2Se_3$ nanowire in Fig. 4 resembles qualitatively the spectrum of

Figure 4 Raman spectroscopy. The Raman spectrum of a single $(Bi_{0.62}Sb_{0.38})_2Se_3$ nanowire was recorded with a laser wavelength of $\lambda = 633$ nm at 2.5 mW/µm^2 on the low frequency side and $\lambda = 800$ nm at 15.3 mW/µm^2 on the high frequency side. The main peak at 156 cm^{-1} comes from a Bi–Se bond vibration. For pure Sb_2Se_3 the Sb–Se vibration is located at 190 cm^{-1}. Thus, Sb doping broadens the peak towards higher frequencies. At 174 cm^{-1} the A_{1g}^2 mode of Bi_2Se_3 appears. It is broadened towards lower frequencies by the Sb dopant. Other Bi_2Se_3 modes are silent. The Bi–Bi bond vibration appears as a smaller peak at 141 cm^{-1}. The two peaks at 58 cm^{-1} and 116 cm^{-1} are Se–Se vibrational modes.

Sb_2Se_3 [41]. All vibrational modes that involve Sb atomic sites are shifted to lower frequencies ν, since the atomic mass m of Bi ($Z = 83$) is higher than that of Sb ($Z = 51$) and $\nu \sim m^{-1}$. Therefore, the spectrum can be explained by substitution of Bi by Sb atoms in the orthorhombic lattice. A peak broadening on the high frequency side of the Bi–Se peak is observed as well. For comparison, the Bi–Se peak of pure Bi_2Se_3 is located at 131 cm^{-1} and the Sb–Se peak of Sb_2Se_3 at ~190 cm^{-1} [41]. No peak was observed above 180 cm^{-1}, thereby ruling out the existence of Sb_2Se_3 in our sample.

Our structural analysis shows that Sb-doped Bi_2Se_3 has an orthorhombic crystal structure in which the Sb substitutes on Bi sites. It is characterized by quasi one-dimensional bands, both structurally and electronically, much different from the layered structure known from pure Bi_2Se_3. The fundamental question is whether or not it is a topological insulator, keeping in mind that orthorhombic Sb_2Se_3 is not a TI.

An ARPES (angle-resolved photo emission spectroscopy) spectrum of the bandstructure along the K–Γ–K direction of a single $(Bi_{0.62}Sb_{0.38})_2Se_3$ nanowire shows a single Dirac cone on the surface in Fig. 5. The feature resides in the gap above the bulk valence band similar to 3D bulk Bi_2Se_3 [4], confirming that orthorhombic $(Bi,Sb)_2Se_3$ is a TI. The V-shaped dispersion is from the surface state band (SSB), and the apex of the V-shaped dispersion indicates the Dirac point. The bandgap of the sample from the experiment is ≥ 200 meV, and the Fermi level E_F of the sample resides at the very bottom of the bulk conduction band, indicating a very low doping level.

4 Discussion and conclusions The incorporation of Sb into Bi_2Se_3 leads to an orthorhombic crystal structure (space group Pnma). Sb enters the crystalline matrix by replacing Bi, as concluded from the shift of the vibrational modes in the Raman spectrum. The amount of Sb doping can be controlled via the substrate temperature during
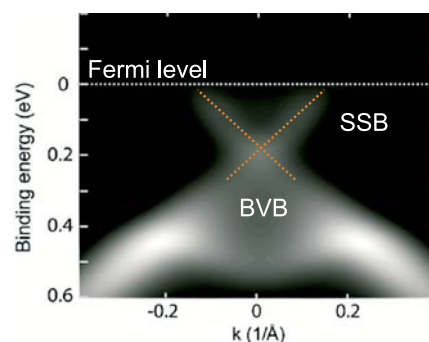

Figure 5 Electronic bandstructure of a $(Bi_{0.62}Sb_{0.38})_2Se_3$ nanowire. The micro-ARPES spectrum along the K–Γ–K direction was taken on an individual nanowire. The energy is measured with respect to the Fermi level. The broad bulk valence band (BVB) is indicated and a bulk bandgap of ≥ 200 meV is visible. The surface state band (SSB) has a distinct V-shape and the crossover point is the Dirac point.

CVD growth. Instead of Au, we employed TiO_2 nanoparticles as a catalyst [16]. We explored the entire temperature range in which doping was possible, starting from Sb-free, binary Bi_2Se_3 at 550 °C down to the lowest temperature (400 °C) at which Sb starts to crystallize out. The Sb doping concentration (in % of the Bi sites) ranges from 0 to 55. Our study focused on the 38% Sb-doped sample. The nanowires are pure, dense, and uniform, which allowed us to study ensembles by X-ray powder diffraction which unambiguously confirms the orthorhombic crystal structure of the nanowires. Previous work found a maximum doping concentration of 10% and the formation of an Sb_2Se_3 guest lattice [27, 28] which was absent in our study in both the TEM and XRD data. In micro-ARPES measurements on an individual nanowire we found a TSS. The bulk bandgap is $\geq$200 meV. The Fermi level resides above the Dirac point and no further surface doping was required to make the TSS visible.

The interesting question is why Sb-doped Bi_2Se_3 with its peculiar quasi one-dimensional sheet structure is a topological insulator, while the end member of the doping series, orthorhombic Sb_2Se_3, is not. A possible reason could be the strain resulting from Sb doping. Starting from the topologically trivial, orthorhombic Sb_2Se_3 structure, the insertion of Bi^{3+} (ionic radius 117 pm, as compared to 90 pm for Sb^{3+}) will lead to an expansion of the lattice, similar to the application of pressure [42, 43]. In the future, density functional theory calculations are planned to better understand the occurrence of the TSS in one-dimensional structures which are very much different from the layered structure of the vast majority of all experimentally confirmed TIs.

Further details of the crystal structure investigation may be obtained from the Fachinformationszentrum Karlsruhe, 76344 Eggenstein-Leopoldshafen (Germany), on quoting the depository number CSD-428739.

References

[1] L. Fu, C. L. Kane, and E. J. Mele, Phys. Rev. Lett. **98**, 106803 (2007).

[2] M. Z. Hasan and C. L. Kane, Rev. Mod. Phys. **82**, 3045–3067 (2010).

[3] G. Brumfiel, Nature **466**, 310–311 (2010).

[4] Y. L. Chen, J.-H. Chu, J. G. Analytis, Z. K. Liu, K. Igarashi, H.-H. Kuo, X. L. Qi, S. K. Mo, R. G. Moore, D. H. Lu, M. Hashimoto, T. Sasagawa, S. C. Zhang, I. R. Fisher, Z. Hussain, and Z. X. Shen, Science **329**, 659–662 (2010).

[5] H. Zhang, C.-X. Liu, X.-L. Qi, X. Dai, Z. Fang, and S.-C. Zhang, Nature Phys. **5**, 438–442 (2009).

[6] H. Peng, K. Lai, D. Kong, S. Meister, Y. Chen, X.-L. Qi, S.-C. Zhang, Z.-X. Shen, and Y. Cui, Nature Mater. **9**, 225–229 (2010).

[7] J. H. Bardarson, P. W. Brouwer, and J. E. Moore, Phys. Rev. Lett. **105**, 156803 (2010).

[8] S. Matsuo, K. Koyama, K. Shimamura, Y. Arakawa, Y. Nishihara, D. Chiba, K. Kobayashi, T. Ono, C.-Z. Chang, K. He, X.-C. Ma, and Q.-K. Xue, Phys. Rev. B **85**, 075440 (2012).

[9] J. J. Cha, K. J. Koski, and Y. Cui, Phys. Status Solidi RRL **7**, 15–25 (2013).

[10] K. W. Kolasinski, Curr. Opin. Solid State Mater. Sci. **10**, 182–191 (2006).

[11] M. E. Messing, K. Hillerich, J. Johansson, K. Deppert, and K. A. Dick, Gold Bulletin **42**, 172–181 (2009).

[12] D. Kong, J. C. Randel, H. Peng, J. J. Cha, S. Meister, K. Lai, Y. Chen, Z.-X. Shen, H. C. Manoharan, and Y. Cui, Nano Lett. **10**, 329–333 (2010).

[13] Y. Yan, Z.-M. Liao, Y.-B. Zhou, H.-C. Wu, Y.-Q. Bie, J.-J. Chen, J. Meng, X.-S. Wu, and D.-P. Yu, Sci. Rep. **3**, 1264 (2013).

[14] J. B. Hannon, S. Kodambaka, F. M. Ross, and R. M. Tromp, Nature **440**, 69–71 (2006).

[15] L. Fang, Y. Jia, D. J. Miller, M. L. Latimer, Z. L. Xiao, U. Welp, G. W. Crabtree, and W.-K. Kwok, Nano Lett. **12**, 6164–6169 (2012).

[16] P. Schönherr, D. Prabhakaran, W. Jones, N. Dimitratos, M. Bowker, and T. Hesjedal, Appl. Phys. Lett. **104**, 253103 (2014).

[17] M. König, S. Wiedmann, C. Brüne, A. Roth, H. Buhmann, L. W. Molenkamp, X. L. Qi, and S. C. Zhang, Science **318**, 766–770 (2007).

[18] D. Hsieh, D. Qian, L. Wray, Y. Xia, Y. S. Hor, R. J. Cava, and M. Z. Hasan, Nature **452**, 970–974 (2008).

[19] D. Hsieh, Y. Xia, D. Qian, L. Wray, J. H. Dil, F. Meier, J. Osterwalder, L. Patthey, J. G. Checkelsky, N. P. Ong, A. V. Fedorov, H. Lin, A. Bansil, D. Grauer, Y. S. Hor, R. J. Cava, and M. Z. Hasan, Nature **460**, 1101–1105 (2009).

[20] Y. Xia, D. Qian, D. Hsieh, L. Wray, A. Pal, H. Lin, A. Bansil, D. Grauer, Y. S. Hor, R. J. Cava, and M. Z. Hasan, Nature Phys. **5**, 398–402 (2009).

[21] Y. L. Chen, J. G. Analytis, J.-H. Chu, Z. K. Liu, S.-K. Mo, X. L. Qi, H. J. Zhang, D. H. Lu, X. Dai, Z. Fang, S. C. Zhang, I. R. Fisher, Z. Hussain, and Z.-X. Shen, Science **325**, 178–181 (2009).

[22] A. Sulaev, P. Ren, B. Xia, Q. H. Lin, T. Yu, C. Y. Qiu, S. Y. Zhang, M. Y. Han, Z. P. Li, W. G. Zhu, Q. Y. Wu, Y. P. Feng, L. Shen, S. Q. Shen, and L. Wang, AIP Advances **3**, 032123 (2013).

[23] A. Barfuss, L. Dudy, M. R. Scholz, H. Roth, P. Höpfner, C. Blumenstein, G. Landolt, J. H. Dil, N. C. Plumb, M. Radovic, A. Bostwick, E. Rotenberg, A. Fleszar, G. Bihlmayer, D. Wortmann, G. Li, W. Hanke, R. Claessen, and J. Schäfer, Phys. Rev. Lett. **111**, 157205 (2013).

[24] C. Brüne, C. X. Liu, E. G. Novik, E. M. Hankiewicz, H. Buhmann, Y. L. Chen, X. L. Qi, Z. X. Shen, S. C. Zhang, and L. W. Molenkamp, Phys. Rev. Lett. **106**, 126803 (2011).

[25] J. G. Analytis, R. D. McDonald, S. C. Riggs, J.-H. Chu, G. S. Boebinger, and I. R. Fisher, Nature Phys. **6**, 960–964 (2010).

[26] Y. Zhang, C.-Z. Chang, K. He, L.-L. Wang, X. Chen, J.-F. Jia, X.-C. Ma, and Q.-K. Xue, Appl. Phys. Lett. **97**, 194102 (2010).

[27] S. S. Hong, J. J. Cha, D. Kong, and Y. Cui, Nature Commun. **3**, 757 (2012).

[28] C. H. Lee, R. He, Z. Wang, R. L. J. Qiu, A. Kumar, C. Delaney, B. Beck, T. E. Kidd, C. C. Chancey, R. M. Sankaran, and X. P. A. Gao, Nanoscale **5**, 4337–4343 (2013).

[29] H. Okamoto, J. Phase Equilibria **15**, 195–201 (1994).

[30] J. W. Earley, Am. Mineral. **35**, 337–364 (1950).

[31] V. G. Kuznetsov and K. K. Palkina, Russ. J. Inorg. Chem. **8**, 624–632 (1963).

[32] G. Neumann and R. Scheidegger, Helv. Phys. Acta **40**, 293–300 (1967).

[33] L. F. Vereshchagin, E. S. Itskevich, E. Ya. Atabaeva, and S. V. Popova, Sov. Phys. – Solid State **6**, 1763–1764 (1965).

[34] N. J. Cook, C. L. Ciobanu, T. Wagner, and C. J. Stanley, Can. Mineral. **45**, 665–708 (2007).

[35] R. Caracas and X. Gonze, Phys. Chem. Minerals **32**, 295–300 (2005).

[36] R. Vadapoo, S. Krishnan, H. Yilmaz, and C. Marin, Nanotechnol. **22**, 175705 (2011).

[37] A. P. Hammersley, FIT2D: An introduction and overview, ESRF Internal Report, 1997.

[38] Bruker AXS (2009): Topas V4.2, 2009.

[39] J. Zhao, H. Liu, L. Ehm, D. Dong, Z. Chen, and G. Gu, J. Phys.: Condens. Matter **25**, 125602 (2013).

[40] T. Zhai, M. Ye, L. Li, X. Fang, M. Liao, Y. Li, Y. Koide, Y. Bando, and D. Golberg, Adv. Mater. **22**, 4530–4533 (2010).

[41] Z. G. Ivanova, E. Cernoskova, V. S. Vassilev, and S. V. Boycheva, Mater. Lett. **57**, 1025–1028 (2003).

[42] I. Efthimiopoulos, J. Zhang, M. Kucway, C. Park, R. C. Ewing, and Y. Wang, Sci. Rep. **3**, 2665 (2013).

[43] W. Liu, X. Peng, C. Tang, L. Sun, K. Zhang, and J. Zhong, Phys. Rev. B **84**, 245105 (2011).

Supporting Information Additional supporting information may be found in the online version of this article at the publisher's website.